Enhancing the charge extraction and stability of perovskite solar cells using strontium titanate ($SrTiO_3$) electron transport layer

Marios Neophytou,[a,†,*] Michele De Bastiani,[a,†] Nicola Gasparini,[a] Erkan Aydin,[a] Esma Ugur,[a] Akmaral Seitkhan,[a] Floriana Moruzzi,[a] Yasmin Choaie,[a] Alexandra J. Ramadan,[b] Joel R. Troughton,[a] Rawad Hallani,[a] Achilleas Savva,[c] Leonidas Tsetseris,[d] Sahika Inal,[c] Derya Baran,[a] Frédéric Laquai,[a] Thomas D. Anthopoulos,[a] Henry J. Snaith,[b] Stefaan De Wolf,[a,*] and Iain McCulloch[a,*]

a) *KAUST Solar Centre (KSC), Division of Physical Science and Engineering (PSE), King Abdullah University of Science and Technology, Thuwal, 23955-6900, Saudi Arabia. E-mail: marios.neophytou@kaust.edu.sa; stefaan.dewolf@kaust.edu.sa; iain.mcculloch@kaust.edu.sa*

b) *Department of Physics, Clarendon Laboratory, Parks Road, Oxford OX1 3PU, United Kingdom.*

c) *Biological and Environmental Science and Engineering, KAUST, Thuwal 23955-6900, Kingdom of Saudi Arabia.*

d) *Department of Physics, National Technical University of Athens, GR15780 Athens, Greece.*

[†] Equally contributed to this work.

Abstract

Charge transport layers strongly influence the performance of perovskite solar cells (PSCs). To date, compact layers and mesoporous scaffolds of titanium dioxide have emerged as good electron transport layers (ETL), enabling record power conversion efficiencies (PCE). However, these ETLs require sintering above 400 °C, which excludes them from low-temperature applications such as flexible devices and silicon-heterojunction tandems. Furthermore, instability of TiO_2 under prolonged exposure to sun light appears to be a critical issue. Here, we present the promising characteristics of low-temperature processed strontium titanate (STO) as an ETL to realize PSCs with 19% PCE. STO is a wide bandgap transparent inorganic perovskite. Compared to other low-temperature processed interlayers, STO reduces the parasitic absorption in the ultraviolet and visible range, improves the electron transport and greatly increases the stability of the devices, retaining ~80% of their initial efficiency after 1000 hours of constant white light illumination.

Introduction

Optimizing the processing conditions of charge-transport layers is a topic of great importance for high-efficiency perovskite solar cells (PSCs). Compact layers and mesoporous scaffolds of titanium dioxide (c-TiO_2 and m-TiO_2, respectively) are among the most often employed candidates for the extraction of photo-generated electrons, enabling solar cell power conversion efficiencies (PCE) now up to 23.7%.[1] For this, TiO_2 typically requires a sintering step of up to ~500 °C to fully crystallize into the desired polymorph.[2] Unfortunately, this high-temperature requirement complicates the fabrication process and limits the application range of PSCs. Furthermore, critical instabilities, specifically under ultraviolet light exposure, have been observed in perovskite cells utilizing TiO_2.[3, 4] These issues motivate the development of low-temperature processed binary (MO_x) and ternary ($M_1M_2O_x$) metal-oxide nanoparticles such as ZnO,[5, 6] SnO_2,[7-9] WO_3,[10] La-$BaSnO_3$,[11-13] and Zn_2SnO_4.[14-16] One effective approach to fabricate a large pool of such oxides is by the combustion synthesis method, which has already been employed for their production for optoelectronic applications.[17] In this method, an oxidizer and fuel are combined in the precursor solution, requiring only mild thermal annealing (in the range of 100-200 °C) to initiate an exothermic reaction within the film. The heat associated with such synthesis provides localized energy supply, eliminating the need for high, externally applied processing temperatures.[18] Of specific interest, La-doped $BaSnO_3$ has recently been shown to be a highly effective n-type charge extraction layer used in perovskite solar cells, and it appears to overcome the UV instability which is otherwise present with TiO_2 charge extraction layers.[13] However, in order to obtain efficient solar cells using La-$BaSnO_3$, Shin *et al.* coated compact TiO_2 with La-$BaSnO_3$ nanoparticles, and subsequently re-sintered the films at 500 °C for one hour. This is therefore incompatible with low temperature processed devices.

In the early stages of PSCs research, strontium titanate ($SrTiO_3$, abbreviated as STO) gathered attention as a possible candidate to replace m-TiO_2 owing to its crystal structure showing similarities with that of common hybrid halide perovskites.[19, 20] In these studies, TiO_2 was used in combination with $SrTiO_3$ that was annealed at high temperatures (450 °C). However, this preliminary research failed to produce devices

with PCEs in excess of 10%, leaving the full potential of STO unrealized. Here, we develop a low temperature processing route to investigate the electron-transport layer (ETL) properties of STO for the realization of efficient and stable PSCs, and compare its performance with devices using TiO_2 nanoparticles (np-TiO_2) as the ETL. We fabricate the STO thin film using a combustion synthesis approach, which yields highly crystalline films with excellent optoelectronic properties and requires only a 150 °C post-deposition annealing. We tailor the synthesis of stand-alone STO in order to achieve PSCs with 19% PCE. We compare the carrier-transport properties of STO to those of other well-known low-temperature processed electron-selective materials. We find that STO not only excels in electron extraction, but also greatly increases the operational lifetime of devices. We believe that this work paves the way for new strategies to realize efficient and stable PSCs for flexible and tandem applications.

Results and discussion

STO is an inorganic perovskite with an average direct electronic bandgap of 3.75 eV, implying that it absorbs much less UV light than the archetypical TiO_2, with a band gap of 3.2 eV.[21-23] STO found use in the growth of superconducting perovskites;[24, 25] its remarkable transparency also makes it attractive for optical applications.[26, 27] The crystal motif consists of Ti^{4+} centered octahedra with oxygen corner-shared anions, within cages of Sr^{2+} cations (see Figure 1a). We synthesize STO powder *via* a low-temperature polymeric matrix approach (see Supporting Information for the details of the synthesis). X-ray diffraction (XRD) analysis of the as-synthesized powder did not feature any Bragg reflections. Differential scanning calorimetry (DSC) was then performed on the as-synthesized powder, showing a strong exothermic reaction when the powder was heated to 150 °C. This is indicative of a combustion reaction between a fuel and oxidizer, yielding film crystallization, and promoting its optoelectronic properties (see Figure S1).[28] XRD measurements of the powder annealed at 150 °C confirmed the presence of a crystalline phase of STO with tetragonal symmetry after several rinsing with a mixture of DMSO/DMF (Figure 1b).[29] The three extra peaks observed in the diffractograms (at 2θ = ~26°, ~37° and ~71°) are attributed to the presence of trace amounts of unreacted precursors such as strontium nitrate. These peaks are more pronounced when the sample is not rinsed

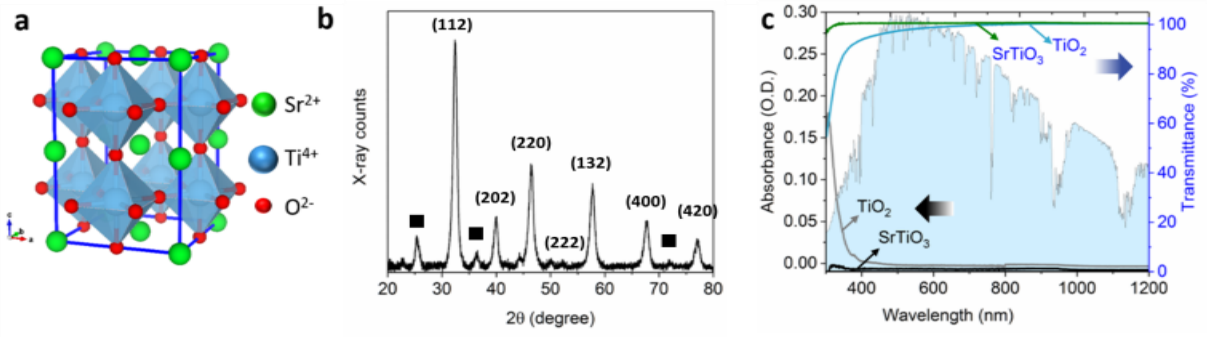

Figure 1. a) Crystal structure of STO in the tetragonal phase. **b)** XRD pattern with the assigned crystallographic directions of STO powder annealed at 150 °C and washed with a DMSO/DMF mixture. The squares indicate the peaks attributed to strontium nitrate. **c)** Absorbance and transmittance spectra of the STO and np-TiO_2 films used to realize PSCs. Black and gray lines: STO and np-TiO_2 absorbance, respectively. Light blue and green lines: np-TiO_2 and STO transmittance, respectively, in the background the AM1.5G spectrum.

(see Figure S2). To further investigate the thermal stability of STO, we performed XRD measurement s at temperatures between room temperature and 350 °C (Figure S3). The reflection patterns clearly indicate that the lattice structure of STO does not change within this temperature range; the only appreciable difference is found in a small shift attributed to thermal expansion.[30]

We fabricated STO thin films by spin-coating a solution of as-synthesized powder dissolved in DMSO, followed by annealing at 150°C to trigger the combustion of the fuel and oxidizers within the solution. The final thickness of the films was ~20nm as measured through profilometry and cross-sectional TEM (see below for more details). As an ETL, STO presents three outstanding characteristics when compared to conventional c-TiO_2. Firstly, STO deposition requires an annealing step at 150 °C, significantly lower than the sintering temperature (~500 °C) required for c-TiO_2 and La-$BaSnO_3$. This reduction in processing temperature is relevant not only to simplify the fabrication process, but also to facilitate the coupling between the perovskite and other solar cells in tandem configurations. This is particularly relevant in the case of tandem silicon heterojunction solar cells, where annealing temperatures in excess of 200 °C are detrimental to the performance of the silicon sub-cell.[31, 32] For these reasons, low-temperature processed TiO_2 layers, mainly comprised of TiO_2 nanoparticles (np-TiO_2), have been explored in previous studies.[33, 34] Thus, to test the performance of STO in *n-i-p* solar cells we have taken low-temperature processed np-TiO_2 as the reference ETL. Secondly, another advantage of STO ETLs is that they result in less parasitic absorption in the visible region of the spectrum compared to np-TiO_2, as also evidenced in Figure 1c which shows the absorbance and transmittance

spectra of the respective films. Notably, STO features negligible absorption in the visible and near-infrared region with an experimental band gap of 4.1 eV (see Figure S4), whereas the np-TiO_2 film shows an absorption edge at ~400 nm which undesirably overlaps with the perovskite absorption. Thirdly, thanks to its similar perovskite structure, STO substrates may be used to template the 'epitaxial' growth of defect-tolerant hybrid halide perovskite films.[19] To illustrate this point, we performed DFT simulations to model the interface between the two perovskites (see Figure 2a and Supporting Information for DFT details). We calculated that the lattice mismatch between the three supercells can be as low as 1% depending on the crystallographic orientation. Figure 2a shows a representation of such a low mismatch interface, wherein the halide perovskite retains the bonding topology of its pseudo-cubic phase, but with a certain degree of disorder (which is also present in the STO part of the interface, albeit to a lesser degree). It may be that this disorder reduces with increasing thickness of the halide perovskite, however the current size of the supercell (250 atoms in total) represents a computational limit at present. Conversely, the interfaces between perovskite and TiO_2 show a lattice mismatch of more than 4%. Here, full relaxation of the interface gives the structure depicted in Scheme S3a, which includes overstretched Pb-I bonds and isolated iodine species closer to the TiO_2 side of the boundary. From this, we can infer that the TiO_2/perovskite interface structure appears to be more defective than its STO/perovskite counterpart. The density of states (DOS) for the TiO_2/perovskite interface model are plotted in Scheme S3b. These results show the presence of a deep state within the energy band gap at the TiO_2/perovskite interface, which may act as a recombination site, deteriorating device performance.

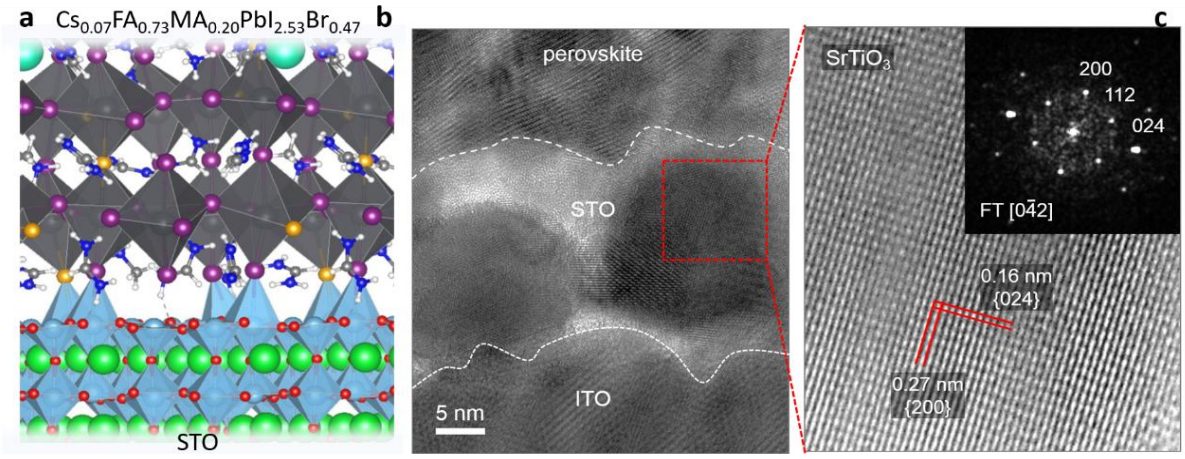

Figure 2. a) Simulation of the interface between the STO and the halide perovskite. **b)** TEM and **c)** HR-TEM images of the cross-sectional interface of ITO/STO/perovskite samples. The inset reports the electron diffraction pattern with the characteristics reflections of STO.

The main findings from the atomic-scale DFT calculations described above on the integrity of the STO and per ovskite parts are consistent with detailed information we obtained about the STO/perovskite interface from high-resolution cross-sectional transmission electron microscopy (HR-TEM) on a focused-ion-beam (FIB) milled sample (Figure 2b). As shown in Figure 2c the STO layer exhibits a long-range order and polycrystalline character with a lattice distance of 0.27 nm and 0.16 nm corresponding to (200) and (024) planes respectively for the tetragonal phase.[29] STO forms a defined, well-aligned interface with both ITO and the halide perovskite. In addition, from the HR-TEM image we infer the STO layer thickness to be in the range of 21-25 nm, in line with the profilometer results.

To realize *n-i-p* solar cells, thin films of STO and np-TiO_2 were deposited as ETLs on pre-cleaned ITO-coated glass substrates.

On each ETL, a triple-cation lead mixed-halide perovskite ($Cs_{0.07}FA_{0.73}MA_{0.20}PbI_{2.53}Br_{0.47}$) film was then deposited to act as the light absorber, covered by spiro-OMeTAD as a hole transport layer (HTL). To complete the device, a 100nm gold electrode was thermally evaporated on top of the HTL. Figure 3a shows a schematic of the structural layers together with a cross-section scanning electron microscopy (SEM) micrograph of the device.

We used ultraviolet photoelectron spectroscopy (UPS) to measure the work function (WF) and valence band maximum (VBM) of both the STO and the perovskite layer (see Figure S5). The resulting energy-level diagram for the STO device is shown in

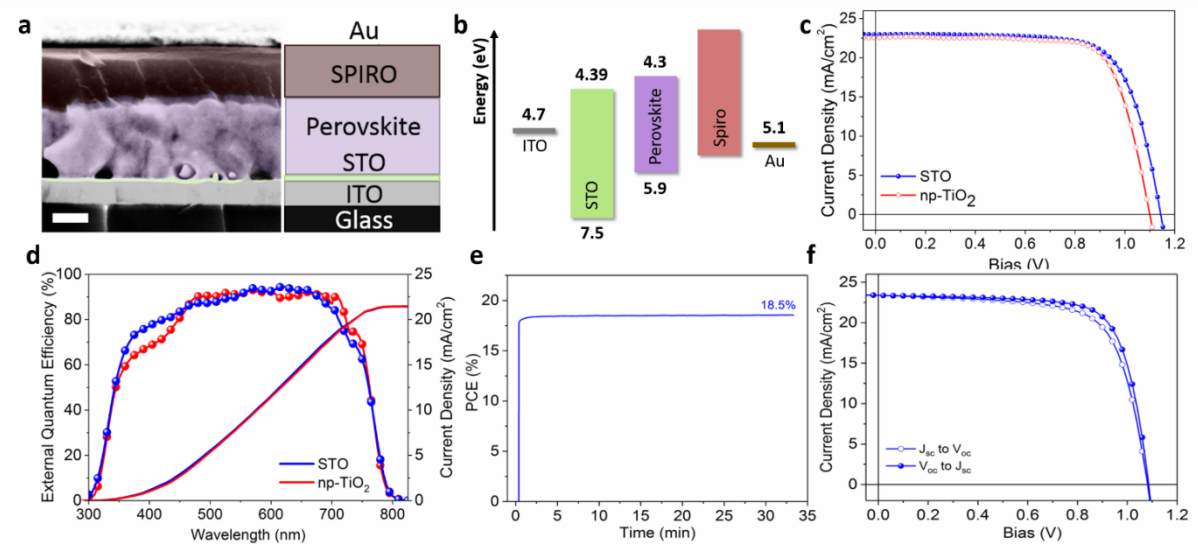

Figure 3. a) Cross-sectional SEM image of the STO device with the structure of the device. White bar: 100 nm. **b)** Energy band diagram of the STO device showing the VB (lower) and WF alignment (upper) measured by UPS. **c)** J-V characteristics of the STO (blue) and np-TiO_2 (red) champion devices. Scan direction from V_{oc} to J_{sc}, scan rate 50 mV/s. **d)** EQE spectra of the STO (blue) and np-TiO_2 (red) champion devices with the respective integrated short-circuit current. **e)** Stabilized PCE and current over 30 min for the STO device. **f)** J-V curves with different scan direction for the STO device functionalized with 3 nm of fullerene.

Figure 3b. As discussed previously, STO is a wide bandgap semiconductor (bandgap of ~4.1 eV), with a VBM of 7.5 eV and a WF of 4.39 eV, as also indicated in the energy diagram. Our STO exhibits slightly higher ban d gap than what has been reported previously in the literature. Such a small deviation can be mainly attributed to the presence of nitrate leftover in the films, even after washing with DMSO/DMF solvent mixture. The relatively low WF combined with its wide bandgap gives it a favorable energetic alignment with the perovskite layer, acting as an efficient ETL and hole blocking layer.

Figure 3c shows the J-V characteristics of STO and np-TiO_2 based solar cells measured at 100 mW cm^{-2} (AM 1.5G). The STO-based device yields improved photovoltaic performance compared to the np-TiO_2 reference with 23 mA/cm^2 J_{sc}, 1143 mV V_{oc}, 72.1 % FF and an overall 19.0 % PCE, compared to 22.62 mA/cm^2 J_{sc}, 1098 mV V_{oc}, 74.3 % FF and a total 18.4 % PCE for the np-TiO_2 device. A substantial reduction of the hysteretic response in the J-V curves can be obtained by evaporating 3 nm of fullerene on top of the STO layer (see Figure 3f and S6). [35-37] To validate our results, we performed a statistical analysis over a set of 25 devices with STO and np-TiO_2 (see Figure S7). On average, the STO-based devices present consistently higher PCEs thanks to better J_{sc} and V_{oc} compared to np-TiO_2 devices, albeit at the expense

of a slight reduction in FF. The narrow distribution of the statistical data is indicative of higher reproducibility in STO devices compared to the np-TiO_2 devices. Table 1 compares the performances of STO and np-TiO_2 champion devices together with the average performances extracted from the statistical analysis.

ETL	**J_{sc} (mA/cm^2)**	**V_{oc} (mV)**	**FF (%)**	**PCE (%)**
STO	23.02	1143	72.1	19.0 (17.98)
np-TiO_2	22.62	1098	74.3	18.4 (17.39)

Table 1. Figures of merit for the STO and np-TiO_2 champion devices. In brackets the average PCE over a batch of 25 devices.

Additional insight about the short-circuit current density of the devices is given by their external quantum efficiency (EQE). As illustrated in Figure 3d, the EQE spectra are well matched with the absorption spectrum of the perovskite layer.[38] The integrated current density is in good agreement with the J-V derived J_{sc} values with a difference below 5%. As expected, we find that in the 350-450 nm range, the quantum efficiency of the STO device is higher compared to the np-TiO_2 device. This enhancement is attributed to the higher optical transparency of the STO layer in this spectral region, avoiding parasitic absorption as is the case with the np-TiO_2 layer.

To gain better insight into the charge extraction properties of STO, we performed time-resolved photoluminescence spectroscopy (TR-PL) on neat perovskite, STO/perovskite, np-TiO_2/perovskite bilayer samples. Figure 4a depicts the PL dynamics of the three films after excitation at 1.91 eV (full details of the measurement can be found in the experimental section). In Figure S8 we show the 2D pseudo-color PL spectra obtained on perovskite, perovskite/STO and perovskite/np-TiO_2 films. The initial charge carrier concentration present after pulsed laser photoexcitation was calculated to be $n_0 = 5.1\times10^{15}$ cm^{-3}, which is in the range of steady-state carrier concentrations expected under 1-sun illumination. We calculate photogenerated carrier lifetimes using a weighted average after a bi-exponential fitting. The average carrier lifetime of the perovskite thin films was 216 ns, while the

lifetimes of the ETL/perovskite junctions were 122 ns and 50 ns for np-TiO_2 and STO, respectively (Figure 3a). The STO/perovskite sample demonstrates a dramatically higher quenching efficiency of 77% compared to pristine perovskite (see Table S1). The reduction of the PL lifetime can be an indication of efficient charge extraction from the perovskite into the transport layer (STO or np-TiO_2) or it can have its origin

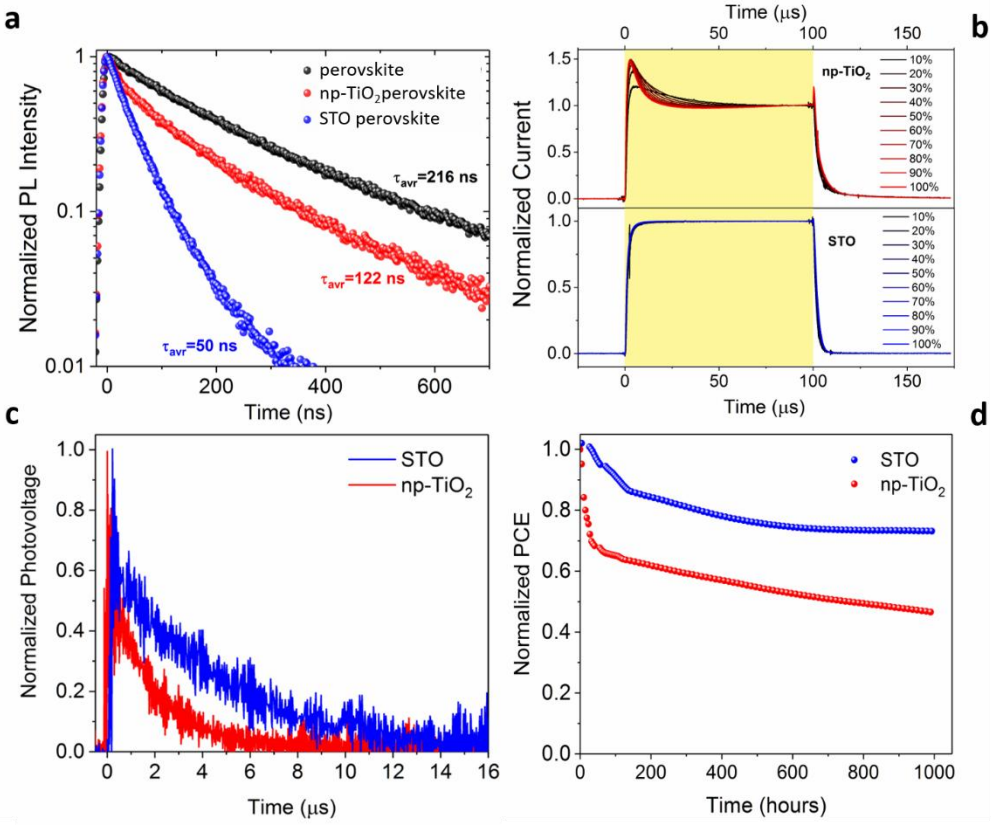

Figure 4. a) TR-PL transient excited at 650 nm of pristine perovskite (black), np-TiO_2/perovskite (red) and STO/perovskite (blue) samples. The lifetime is calculated from the average of the bi-exponential fitting. **b)** Normalized TPC results on the np-TiO_2 (red, top) and STO (blue, bottom) devices at different light intensity (100% = 1.1 suns). The yellow square represents the light pulse. **c)** TPV results on the np-TiO_2 (red) and STO (blue) devices. **d)** Stability of STO (blue) and np-TiO_2 based (red) perovskite devices under constant illumination (1 sun) and in inert environment.

in increased interfacial recombination.[39] In fact, extraction of electrons (or holes) from the photoactive layer to the charge transport layer or trapping of carriers at the interface compete with radiative recombination in the photoactive layer, thereby reducing the observed PL lifetime.[40] Moreover, non-radiative losses due to defects either in the bulk of the perovskite or at the ETL/perovskite (or HTL/perovskite) interface cause a drop in V_{oc} for perovskite solar cells.[41, 42] However, here we obtain higher V_{oc} values up to 1143 mV when STO is employed as an ETL. Therefore, we attribute the faster PL decay of the STO/perovskite bilayer sample with respect to the np-TiO_2/perovskite bilayer film to electron extraction from the perovskite to the STO.

The absolute PL quenching does not necessarily imply an increased non-radiative recombination rate, but is likely to be a consequence of a rapid depopulation of electron density within the perovskite absorber layer, which reduces the total radiative bimolecular recombination rate, which is proportional to the product of the electron and hole number density. To further validate these hypotheses, we utilized transient photocurrent (TPC) measurements to probe the dynamics of carrier injection/extraction in PSCs.[43] Figure 4b shows the TPC results at short-circuit for the np-TiO_2 (top) and STO (bottom) devices, at different light intensities. In the early microsecond region, the np-TiO_2 device exhibits an increase in photocurrent with an intensity proportional to the light irradiation. This anomaly is attributed to non-ideal charge-extraction and carrier-accumulation at the interface.[44] Moreover, we note that the time evolution of this phenomenon is linked to the intensity of the irradiation, i.e., higher illumination conditions result in faster decay. These observations suggest that the np-TiO_2 layer slows down the extraction of photo-induced electrons and favours carrier recombination at the np-TiO_2/perovskite interface, possibly through the defect level identified by DFT calculations (see above). This behaviour is absent in the STO device: here, the TPC transient rises monotonously and stabilizes within ~10 µs, independent of light irradiation, indicating efficient injection of the photo-generated carriers into the STO layer. Similar conclusions can be drawn from observing the decay of TPC transients at 100 µs (see Figure S9). Indeed, in the np-TiO_2 device, the photocurrent decay extend up to ~30 µs after the turn-off of the light pulse (the on/off time resolution of the light excitation is tens of nanoseconds, see experimental section for more details), which again confirms poor extraction properties of the np-TiO_2 layer. Additionally, since 30 µs is much longer than the intrinsic lifetime we expect from the perovskite absorber layer, we suspect that a slow de-trapping of trapped carriers is responsible for this slow decay. On the other hand, the decay time of the photocurrent in the STO device is reduced to ~10 µs, which confirms the aforementioned enhanced extraction properties of the layer, and is consistent with fewer or shallower electron traps in the STO containing devices.

The fast transient response in STO-based devices together with the higher V_{oc} compared to np-TiO_2 based devices can be linked to a reduction of the trap density at

the ETL/perovskite interface.[45] To support this, we performed transient photovoltage (TPV) measurements under 1-sun conditions. Figure 4c shows the normalized photovoltage as a function of time after excitation for the perovskite devices. We calculate a charge carrier lifetime (τ_l) of 8.7 µs and 4.1 µs for STO and np-TiO_2 based devices, respectively. The longer τ_l obtained for STO devices reflects a reduction in interfacial recombination in devices, leading to a slightly higher V_{oc} (see Figure S7).
Finally, to investigate the photostability of the devices and their performance, we placed the solar cells in a nitrogen-filled chamber and irradiated continuously at an equivalent AM1.5 irradiance of 100 mW/cm^2, with the illumination generated from white light LEDs. We show the spectrum in the SI and note that it does not contain significant intensity below 400nm. [46, 47] Figure 4d depicts the time-dependent PCE evolution of STO and np-TiO_2 based solar cells. Notably, devices employing STO as the ETL exhibit improved photostability over 1000 hours (PCE loss of 27%) compared to np-TiO_2 solar cells whose efficiency majorly degraded over the same period (PCE loss of 54%). These results demonstrate that not only is the initial performance improved in STO-based solar cells, but also they possess improved photo-stability compared to np-TiO_2-based devices.

Conclusions

In summary, we present promising photo-extraction properties of STO in PSCs with an *n-i-p* configuration. Utilizing an improved understanding of material synthesis, properties, and device fabrication, we increase the efficiency of STO-based PSCs up to 19%. We find that STO represents a suitable candidate for low-temperature processed ETL in perovskite devices, thanks to its remarkable transparency and efficient photo-electron extraction capabilities. Finally, STO devices present an enhancement in V_{oc} with improved stability of photovoltaic performance, which we attribute to a reduction of interfacial trap states, induced by the STO's epitaxial structure. We believe that the STO which we have presented represents a viable inorganic n-type charge extraction layer, which represents a major breakthrough on the path towards industrially stable perovskite solar cells.

Materials and Methods

Temperature-depended Powder X-ray diffraction (XRD): Diffractograms of precursor powder were taken in ambient air. The temperature was varied from room temperature up to 350 °C with 50 °C steps. Before the measurement the powders were annealed at 150 °C for 1 hour, in a similar way with the films.

Differential Scanning Calorimetry (DSC): The thermal behavior of $SrTiO_3$ was investigated by differential scanning calorimetry using a Discovery DSC (TA) instrument operated at a scanning rate of 20 °C min^{-1} in an interval of 40 °C to 300°C.

UV-Vis characterization: Transmittance and absorbance spectra of the films were recorded using an ultraviolet-visible-near infrared (UV–Vis–NIR) spectrometer (Cary 7000) equipped with integrating sphere. Measurement range was between 300 and 1200 nm. For measurements, the samples were prepared on polished soda lime glasses.

Transmission electron microscopy (TEM): $SrTiO_3$ and perovskite films were deposited sequentially on ITO glass substrates as previously described. The lamella was prepared with the help of a focused ion beam in a scanning electron microscope (Helios 400s, FEI) equipped with a nano-manipulator (Omniprobe, AutoProbe300). To protect the surface of the sample, layers of carbon and platinum were sequentially deposited under electron and ion beams. Gallium ion beam (30 kV, 9 nA) was used first to mill the bulk and then cut the lamella out of the sample. The lamella was then attached to a copper grid in accordance with the lift-out method. Then, the lamella was thinned down with the ion beam reducing the current at each step (30 kV, 2.8 nA – 93 pA). Finally, the lamella was cleaned from the possible contamination with the ion beam at 5 kV, 48 pA and 2 kV, 16 pA. The lamella was then imaged with the transmission electron microscope (Titan 80-300, FEI) at 300 kV operating voltage.

Scanning electron microscopy (SEM): SEM micrographs were collected at 5 kV accelerating voltage with 30 µm beam aperture, using a Zeiss Auriga microscope equipped with an in-lens detector.

Device fabrication and characterization: Pre-patterned ITO glass substrates were in sequence cleaned with soap, acetone and isopropyl alcohol in an ultrasonic bath and dried with N_2. $SrTiO_3$ films were spin cast from DMSO solutions at various

concentrations (ranging from 40-100 mg/mL). Films were annealed in ambient air at 150 °C for 1 hour. Where reported, to reduce the hysteresis 3 nm of C_{60} were thermally evaporated on top of the ETL (see Table S2). The perovskite film was then deposited from a dimethylformamide:dimethyl sulfoxide (DMF: DMSO) solvent mixture. In brief, 1.02 mmol of PbI_2, 0.18 mmol of $PbBr_2$, 0.06 mmol of CsI, 0.17 mmol of MABr, 0.97 mmol of FAI were dissolved in 0.8 ml of DMF and 0.2 ml of DMSO. Chlorobenzene was used as an antisolvent. Substrates were then annealed at 100 °C for 10 minutes. Spiro-OMeTAD layers were deposited via spin coating at 4250 rpm with a ramp of 4250 rpm/s for 30 s, where the Spiro-OMeTAD solution was prepared by dissolving 72.5 mg Spiro-OMeTAD, 28.5 uL 4-tert-butylpyridine and 17.5 µL lithium (trifluoromathensulfonyl)imide solution (520 mg/ml in acetonitrile) in 1 mL chlorobenzene. The substrates were placed in a humidity-control box for >12 hours to ensure sufficient oxidation of the Spiro-OMeTAD. Finally, ~100 nm gold was thermally evaporated through a shadow mask to define an active area of 0.1 cm^2.

The current density-voltage characteristics of perovskite solar cells were measured in a N_2 purged glovebox under standard simulated AM1.5 illumination using a solar simulator (Wavelabs sinus/70) equipped with Keithley 2400. Measurements were done using a custom-built measurement stage without aperture mask at room temperature. The light intensity is 100 mW/cm^2 as checked with a calibrated reference solar cell (RERA Technologies). Scanning rate was 50 mV s^{-1} and voltage step was 10 mV. No preconditioning protocol has been used before the characterization. The reverse scan was from 1.2 V to -0.1V, and the forward scan was from -0.1 V to 1.2 V.

Ultraviolet photoelectron spectroscopy (UPS): UPS measurements were recorded using a SPECS PHOIBOS 100 hemispherical electron energy analyzer in a custom built ultrahigh vacuum (UHV) system with a base pressure of ~1 x 10^{-10} mbar. Samples were excited at 21.21 eV using a He I plasma source.

Time-resolved photoluminescence spectroscopy (TR-PL): TR-PL measurements were conducted using a high-resolution streak camera system (Hamamatsu, C10910). The excitation beam was generated from an optical parametric oscillator (OPO) (Inspire OPO, Radiantis) itself pumped by an fs oscillator (Spectra Physics Mai Tai) at a wavelength of 830 nm. The beam was routed through a pulse picker (*pulse*Select**,**

A·P·E) for repetition rate division. The excitation beam at 650 nm was focused to pump the perovskite samples, mounted inside the sealed chamber. The associated PL emission was spectrally and temporally resolved using a spectrograph and streak camera system. The photogenerated carrier concentration at t=0 was calculated using the formula:

$$n_0 = \frac{\alpha . f}{E_{photon}},$$

where α is the absorption coefficient at the excitation wavelength, f is the fluence of the laser and E_{photon} is the photon energy. Perovskite thin films and electron transport layers for TR-PL spectroscopy measurements were deposited on cleaned quartz substrates using the same protocol as used for the device fabrication. After deposition of the layers, samples were placed in a sealed nitrogen chamber to prevent any changes due to exposure to oxygen and humidity. All measurements were done at room temperature.

Transient photocurrent (TPC): TPC measurements were collected using the all-in-one measurement system PAIOS 3.2 (Fluxim). PAIOS exploits a first function generator to control the light source (a calibrated white LED with a rise/fall time of 100 ns), and a second function generator to control the applied voltage bias. The output current is measured through a trans-impedance amplifier.

Transient photovoltage (TPV): A 405 nm laser-diode was settled for keeping the solar cells in approximately V_{oc} condition. Driving the laser intensity with a waveform generator Agilent 33500B and measuring the light intensity with a highly linear photodiode allowed to reproducibly adjust the light intensity with an error below 0.5% over a range of 0.2 to 4 suns. A small perturbation was induced with a second laser diode driven by a function generator from Agilent. The intensity of the short (50 ns) laser pulse was adjusted to keep the voltage perturbation below 10 mV, typically at 5 mV. After the pulse, the voltage decays back to its steady state value in a single exponential decay. The characteristic decay time was determined from a linear fit to a logarithmic plot of the voltage transient and returned the small perturbation charge carrier lifetime.

Device stability: For devices stability evaluation we used an in-house built degradation setup. The degradation chamber consists of gas in and outlets and electrical contacts for tracking the J-V performance of max 54 solar cells (9 substrates, 6 solar cells per substrate) every 5 minutes. Between each measurement the devices were kept under constant illumination at open-circuit voltage condition. The chamber was kept under nitrogen with a continuous flow of 1 LPM. The degradation chamber is positioned under the LEDs used for light soaking experiments. The intensity of the LEDs was adjusted to give the same short circuit current as under an AM1.5G solar simulator.

Conflicts of interest

There are no conflicts to declare.

Acknowledgements

The research reported in this publication was supported by funding from King Abdullah University of Science and Technology (KAUST). Authors would like to acknowledge financial support from EC FP7 Project SC2 (610115) and EPSRC Projects EP/G037515/1 and EP/M005143/1. This work, was also supported by computational time granted from the Greek Research & Technology Network (GRNET) in the National HPC facility – ARIS – under project pr004034-STEM. The authors acknowledge Dr. Muhammed Sajjad and Dr. Ahmed Mansour for the useful discussion regarding the STO structure.

References

1. NREL, *Best research-cell efficiencies*, 2019.
2. J. M. Ball, M. M. Lee, A. Hey and H. J. Snaith, *Energy & Environmental Science*, 2013, **6**, 1739-1743.
3. T. Leijtens, G. E. Eperon, S. Pathak, A. Abate, M. M. Lee and H. J. Snaith, *Nature Communications*, 2013, **4**, 2885.

4. K. Wojciechowski, T. Leijtens, S. Siprova, C. Schlueter, M. T. Hörantner, J. T.-W. Wang, C.-Z. Li, A. K. Y. Jen, T.-L. Lee and H. J. Snaith, *The Journal of Physical Chemistry Letters*, 2015, **6**, 2399-2405.
5. P. Zhang, J. Wu, T. Zhang, Y. Wang, D. Liu, H. Chen, L. Ji, C. Liu, W. Ahmad, Z. D. Chen and S. Li, *Advanced Materials*, 2018, **30**, 1703737.
6. J. Dong, Y. Zhao, J. Shi, H. Wei, J. Xiao, X. Xu, J. Luo, J. Xu, D. Li, Y. Luo and Q. Meng, *Chemical Communications*, 2014, **50**, 13381-13384.
7. Q. Jiang, L. Zhang, H. Wang, X. Yang, J. Meng, H. Liu, Z. Yin, J. Wu, X. Zhang and J. You, *Nature Energy*, 2016, **2**, 16177.
8. J. Barbé, M. L. Tietze, M. Neophytou, B. Murali, E. Alarousu, A. E. Labban, M. Abulikemu, W. Yue, O. F. Mohammed, I. McCulloch, A. Amassian and S. Del Gobbo, *ACS Applied Materials & Interfaces*, 2017, **9**, 11828-11836.
9. M. Abulikemu, M. Neophytou, J. M. Barbé, M. L. Tietze, A. El Labban, D. H. Anjum, A. Amassian, I. McCulloch and S. Del Gobbo, *Journal of Materials Chemistry A*, 2017, **5**, 7759-7763.
10. K. Mahmood, B. S. Swain, A. R. Kirmani and A. Amassian, *Journal of Materials Chemistry A*, 2015, **3**, 9051-9057.
11. L. Zhu, Z. Shao, J. Ye, X. Zhang, X. Pan and S. Dai, *Chemical Communications*, 2016, **52**, 970-973.
12. S. Sallis, D. O. Scanlon, S. C. Chae, N. F. Quackenbush, D. A. Fischer, J. C. Woicik, J.-H. Guo, S. W. Cheong and L. F. J. Piper, *Applied Physics Letters*, 2013, **103**, 042105.
13. S. S. Shin, E. J. Yeom, W. S. Yang, S. Hur, M. G. Kim, J. Im, J. Seo, J. H. Noh and S. I. Seok, *Science*, 2017, DOI: 10.1126/science.aam6620.
14. S. S. Mali, C. S. Shim, H. Kim and C. K. Hong, *Journal of Materials Chemistry A*, 2016, **4**, 12158-12169.
15. A. Bera, A. D. Sheikh, M. A. Haque, R. Bose, E. Alarousu, O. F. Mohammed and T. Wu, *ACS Applied Materials & Interfaces*, 2015, **7**, 28404-28411.
16. S. S. Shin, W. S. Yang, J. H. Noh, J. H. Suk, N. J. Jeon, J. H. Park, J. S. Kim, W. M. Seong and S. I. Seok, *Nature Communications*, 2015, **6**, 7410.
17. M.-G. Kim, M. G. Kanatzidis, A. Facchetti and T. J. Marks, *Nature Materials*, 2011, **10**, 382.

18. M.-G. Kim, J. W. Hennek, H. S. Kim, M. G. Kanatzidis, A. Facchetti and T. J. Marks, *Journal of the American Chemical Society*, 2012, **134**, 11583-11593.
19. A. Bera, K. Wu, A. Sheikh, E. Alarousu, O. F. Mohammed and T. Wu, *The Journal of Physical Chemistry C*, 2014, **118**, 28494-28501.
20. Y. Okamoto, R. Fukui, M. Fukazawa and Y. Suzuki, *Materials Letters*, 2017, **187**, 111-113.
21. A. H. Kahn and A. J. Leyendecker, *Physical Review*, 1964, **135**, A1321-A1325.
22. M. Cardona, *Physical Review*, 1965, **140**, A651-A655.
23. K. v. Benthem, C. Elsässer and R. H. French, *Journal of Applied Physics*, 2001, **90**, 6156-6164.
24. R. K. Singh and J. Narayan, *Journal of Applied Physics*, 1990, **67**, 3785-3790.
25. R. W. Simon, C. E. Platt, A. E. Lee, G. S. Lee, K. P. Daly, M. S. Wire, J. A. Luine and M. Urbanik, *Applied Physics Letters*, 1988, **53**, 2677-2679.
26. J. M. Marx, O. Eknoyan, H. F. Taylor, Z. Tang and R. R. Neurgaonkar, *Applied Physics Letters*, 1995, **67**, 1381-1383.
27. W. D. Rice, P. Ambwani, M. Bombeck, J. D. Thompson, G. Haugstad, C. Leighton and S. A. Crooker, *Nature Materials*, 2014, **13**, 481.
28. G. Saito, Y. Nakasugi, N. Sakaguchi, C. Zhu and T. Akiyama, *Journal of Alloys and Compounds*, 2015, **652**, 496-502.
29. T. Yamanaka, N. Hirai and Y. Komatsu, *American Mineralogist*, 2002, **87**, 1183-1189.
30. R. A. Cowley, *Physical Review*, 1964, **134**, A981-A997.
31. W. Liu, L. Zhang, R. Chen, F. Meng, W. Guo, J. Bao and Z. Liu, *Journal of Applied Physics*, 2016, **120**, 175301.
32. J. Werner, C.-H. Weng, A. Walter, L. Fesquet, J. P. Seif, S. De Wolf, B. Niesen and C. Ballif, *The Journal of Physical Chemistry Letters*, 2016, **7**, 161-166.
33. J. Y. Kim, S. H. Kim, H.-H. Lee, K. Lee, W. Ma, X. Gong and A. J. Heeger, *Advanced Materials*, 2006, **18**, 572-576.
34. H. Tan, A. Jain, O. Voznyy, X. Lan, F. P. García de Arquer, J. Z. Fan, R. Quintero-Bermudez, M. Yuan, B. Zhang, Y. Zhao, F. Fan, P. Li, L. N. Quan, Y. Zhao, Z.-H. Lu, Z. Yang, S. Hoogland and E. H. Sargent, *Science*, 2017, DOI: 10.1126/science.aai9081.

35. K. Wojciechowski, S. D. Stranks, A. Abate, G. Sadoughi, A. Sadhanala, N. Kopidakis, G. Rumbles, C.-Z. Li, R. H. Friend, A. K. Y. Jen and H. J. Snaith, *ACS Nano*, 2014, **8**, 12701-12709.

36. M. De Bastiani, G. Dell'Erba, M. Gandini, V. D'Innocenzo, S. Neutzner, A. R. S. Kandada, G. Grancini, M. Binda, M. Prato, J. M. Ball, M. Caironi and A. Petrozza, *Advanced Energy Materials*, 2016, **6**, 1501453.

37. C. Tao, S. Neutzner, L. Colella, S. Marras, A. R. Srimath Kandada, M. Gandini, M. D. Bastiani, G. Pace, L. Manna, M. Caironi, C. Bertarelli and A. Petrozza, *Energy & Environmental Science*, 2015, **8**, 2365-2370.

38. S. De Wolf, J. Holovsky, S.-J. Moon, P. Löper, B. Niesen, M. Ledinsky, F.-J. Haug, J.-H. Yum and C. Ballif, *The Journal of Physical Chemistry Letters*, 2014, **5**, 1035-1039.

39. M. D. Bastiani, V. D'Innocenzo, S. D. Stranks, H. J. Snaith and A. Petrozza, *APL Materials*, 2014, **2**, 081509.

40. S. D. Stranks, G. E. Eperon, G. Grancini, C. Menelaou, M. J. P. Alcocer, T. Leijtens, L. M. Herz, A. Petrozza and H. J. Snaith, *Science*, 2013, **342**, 341-344.

41. W. Tress, N. Marinova, O. Inganäs, M. K. Nazeeruddin, S. M. Zakeeruddin and M. Graetzel, *Advanced Energy Materials*, 2015, **5**, 1400812.

42. S. D. Stranks, *ACS Energy Letters*, 2017, **2**, 1515-1525.

43. R. A. Belisle, W. H. Nguyen, A. R. Bowring, P. Calado, X. Li, S. J. C. Irvine, M. D. McGehee, P. R. F. Barnes and B. C. O'Regan, *Energy & Environmental Science*, 2017, **10**, 192-204.

44. I. Hwang, C. R. McNeill and N. C. Greenham, *Journal of Applied Physics*, 2009, **106**, 094506.

45. J. Peng, Y. Wu, W. Ye, D. A. Jacobs, H. Shen, X. Fu, Y. Wan, T. Duong, N. Wu, C. Barugkin, H. T. Nguyen, D. Zhong, J. Li, T. Lu, Y. Liu, M. N. Lockrey, K. J. Weber, K. R. Catchpole and T. P. White, *Energy & Environmental Science*, 2017, **10**, 1792-1800.

46. N. Gasparini, M. Salvador, S. Strohm, T. Heumueller, I. Levchuk, A. Wadsworth, J. H. Bannock, J. C. de Mello, H.-J. Egelhaaf, D. Baran, I. McCulloch and C. J. Brabec, *Advanced Energy Materials*, 2017, **7**, 1700770.

47. D. Baran, N. Gasparini, A. Wadsworth, C. H. Tan, N. Wehbe, X. Song, Z. Hamid, W. Zhang, M. Neophytou, T. Kirchartz, C. J. Brabec, J. R. Durrant and I. McCulloch, *Nature Communications*, 2018, **9**, 2059.